

The electrochemical Na intercalation/extraction mechanism of ultrathin cobalt(II) terephthalate-based MOF nanosheets revealed by synchrotron X-ray absorption spectroscopy

Chao Li^{a,1}, Qi Yang^{a,1}, Ming Shen^a, Jingyuan Ma^{b,*}, Bingwen Hu^{a,*}

^a State Key Laboratory of Precision Spectroscopy, Shanghai Key Laboratory of Magnetic Resonance, Institute of Functional Materials, School of Physics and Materials Science, East China Normal University, Shanghai 200062, PR China

^b Shanghai Synchrotron Radiation Facility, Shanghai Institute of Applied Physics, Chinese Academy of Sciences, Shanghai 201204, PR China

ARTICLE INFO

Keywords:

Metal-organic frameworks
Anode
Sodium-ion batteries
Local electric field
Charge compensation mechanism

ABSTRACT

The discovery of novel metal-organic frameworks with high anodic performance and the in-depth investigation on their charge compensation mechanism is of primary significance to boost their application in sodium-ion batteries. Herein, cobalt(II) terephthalate-based MOF nanosheets (termed “u-CoOHtp”) with oxygen vacancies generated were fabricated via an expedient ultrasonic approach and evaluated as an active anode in Na-ion coin cells for the first time. The oxygen vacancies in u-CoOHtp could induce local built-in electric field, which is able to accelerate ion diffusion rate and thus promote reversible Na⁺ storage. As expected, the obtained u-CoOHtp can deliver a reversible capacity of 555 mA h g⁻¹ at 50 mA g⁻¹ and maintain remarkable cycling performance. More importantly, the valence state and local environment evolution of u-CoOHtp during Na⁺ intercalation/extraction were studied by a combination of hard and soft X-ray absorption spectroscopy (Co and O K-edge). The results substantiate that: (i) the pristine u-CoOHtp is converted to a mixed phase containing Co-MOF, CoO_x species (0 < x < 1) and nanosized Co⁰ after the first cycle; (ii) Co²⁺ and metallic Co are interchangeable during repeated Na⁺ intercalation/extraction; (iii) a certain portion of charge compensation during cycling is achieved on the carboxyl oxygen sites.

1. Introduction

In response to the environmental concerns and ever-increasing energy demands, sodium-ion batteries (SIBs) have recently attracted paramount interest as a promising alternative for lithium-ion batteries (LIBs) due to the huge availability and geographical even distribution of sodium resources [1–3]. Unfortunately, most of the advanced anode materials for LIBs cannot show equally superior electrochemical performance in SIBs due to sodium's unique characteristics, such as large ionic radius (Na⁺: 1.06 Å, versus Li⁺: 0.76 Å) [4–8]. Hence, a great effort for advancing SIBs is the development of anode hosts with high reversible capacity and excellent power performance.

Metal-organic frameworks (MOFs) represent an unique class of organic–inorganic hybrid porous crystalline materials [9–11]. Benefitting from their advantageous characteristics including controllable chemistry and functionality, regular ion diffusion channels, and abundant electroactive constituents, MOFs have attracted tremendous attention in the field of Li-based batteries (Li-ion, Li–air, and Li–S

batteries) [12–24] and electrochemical capacitors [25–28] in recent years. However, only a few MOFs were reported as either cathode or anode materials for SIBs until now [29–31], and their Na-storage performances are still insufficient to meet the demand of future electric vehicles (EVs) and personal electronics. Furthermore, the lack of in-depth investigation on the charge compensation mechanism during Na⁺/Li⁺ intercalation/extraction leaves many important issues unanswered for MOFs, such as whether the structure is reversible, whether the metal ions are participated in the redox reaction, and what is the role of organic ligand. In many cases, MOFs-based electrode materials would become amorphous during the repeated electrochemical process [14,17,24,30,32–36], which limit the use of X-ray diffraction (XRD) and transmission electron microscopy (TEM) techniques that need long-range ordering. Hence, high-resolution characterization techniques that sensitive to atomic short-range ordering including synchrotron hard X-ray absorption fine structure (XAFS) spectroscopy and soft X-ray absorption spectroscopy (sXAS), electron paramagnetic resonance (EPR), and solid-state NMR (SSNMR) spectroscopy [37,38], are

* Corresponding authors.

E-mail addresses: majingyuan@sinap.ac.cn (J. Ma), bwhu@phy.ecnu.edu.cn (B. Hu).

¹ The two authors contribute equally to this work.

expected to be applied in the study of MOFs' structural evolution during cycling.

Herein, cobalt(II) terephthalate-based MOF nanosheets (termed “u-CoOHtp”) were fabricated from an ingenious ultrasonic procedure and evaluated as an anode material in SIBs for the first time. Intriguingly, self-adaptive oxygen vacancies were generated due to the presence of coordinatively unsaturated metal sites on the exposed surfaces of u-CoOHtp, which would cause imbalanced charge distribution and then create local built-in electric field, thus accelerating Na⁺ migration rates and promoting the charge transfer behavior. On the grounds of the multiple structural advantages, the present u-CoOHtp is able to deliver a reversible capacity of 555 mA h g⁻¹ at 50 mA g⁻¹ and maintain outstanding cyclic performance. More importantly, the electronic state and local environment of cobalt and oxygen in the Na⁺ intercalated/extracted u-CoOHtp electrodes were studied by a combination of XAFS and sXAS analysis, which provides an in-depth understanding of the charge compensation mechanism at atomic level for MOFs during the Na⁺ intercalation/extraction processes.

2. Experimental section

2.1. Synthesis of b-CoOHtp and u-CoOHtp MOFs

All the reagents and solvents were purchased from commercial suppliers and used without further purification. The Co₂(OH)₂tp bulk MOF (termed “b-CoOHtp”) was fabricated through a microwave-assisted solvothermal reaction using a microwave-hydrothermal parallel synthesizer (XH-8000, Beijing Xiang Hu Sci & Tech Development Co., LTD). Firstly, 1.50 mmol cobalt chloride hexahydrate (CoCl₂·6H₂O, 0.357 g) and 0.75 mmol terephthalic acid (H₂tp, 0.25 g) were successively dissolved in a mixed solvent of dimethylformamide (DMF, 34 mL), ethanol (10 mL), and water (10 mL). Afterwards, the above solution (*solution A*) was transferred to a polytetrafluoroethylene (PE) high-pressure autoclave and then placed in the microwave synthesizer with magnetic stirring. The heating-up time and temperature retention time were set to be 20 min and 8 h, respectively. After cooling down to room temperature, the resultant crystalline materials were collected by pumping filtration and washed with DMF and water for 3–6 times. Finally, the purple b-CoOHtp product was harvested by vacuum desiccation at 110 °C for 12 h.

The preparation process of Co₂(OH)₂tp ultrathin nanosheets (termed “u-CoOHtp”) was similar to that of b-CoOHtp, except that the reaction was carried out by an ultrasonic procedure using an ultrasonic apparatus (H5200E, Hechuang Ultrasonic Co., LTD). In that case, 1.6 mL trimethylamine (TEA) was injected into the *solution A* and ultrasonicated for several minutes to obtain a uniform colloidal suspension. TEA can act as an alkali to assist the deprotonation of H₂tp ligand and a complexing agent to form ultrathin nanosheets [16,39]. Then, the reaction was performed under 40 kHz for 8 h under airtight condition.

2.2. Materials characterization

The morphology and microstructure of b-CoOHtp and u-CoOHtp MOFs were analyzed by a scanning electron microscopy (SEM, HITACHI, S-4800), a transmission electron microscopy (TEM, FEI, Tecnai G2 F20), and an atomic force microscopy (AFM, Veeco, Multimode-V). The structure of b-CoOHtp and u-CoOHtp MOFs was characterized by a Holland Panalytical PRO PW3040/60 X-ray diffractometer (XRD, Cu-Kα radiation source, λ = 1.5418 Å) and Fourier transform infrared spectrometer (FT-IR, Nicolet, Nexus 670). The thermal behavior was examined by a simultaneous thermo-analyzer (TGA, NETZSCH, STA 449 F3 Jupiter[®]) at a heating rate 10 °C/min under N₂ atmosphere. The porosity was evaluated by an Autosorb-IQ automated gas sorption analyser (N₂ sorption isotherms, 77 K), the specific surface area was determined through Brunauer-Emmett-Teller

(BET) method. The chemical states of elements were evaluated by an ESCALAB 250Xi X-ray photoelectron spectrometer (XPS, Al-Kα radiation, hv = 1486.6 eV). Continuous-wave X-band electron paramagnetic resonance (EPR) spectra were performed at 2 K with a Bruker EMX plus 10/12 spectrometer.

2.3. Electrochemical measurements

The electrochemical properties were investigated with CR2032 coin cells in an argon-filled glovebox (O₂ ≤ 0.1 ppm, H₂O ≤ 0.1 ppm). The working electrodes were composed of the as-synthesized b-CoOHtp and u-CoOHtp materials, acetylene black, and carboxymethyl cellulose (CMC) binder in a weight ratio of 60:30:10. The mass loading of active materials was 1.0–1.2 mg cm⁻². Sodium disks were employed as both counter and reference electrode. Whatman glassy fiber (GF-D) was employed as the separator. The electrolyte was made up with 1 M NaSO₃CF₃ dissolved in diglyme (DGM). Galvanostatic charge/discharge measurements were conducted over a potential range of 0.01–3.00 V vs. Na⁺/Na on a LAND CT2001A battery testing system. All the gravimetric capacities were determined based on the mass of b-CoOHtp or u-CoOHtp. Cyclic voltammetry (CV) was conducted using a CHI 660a electrochemical workstation in the potential window of 0.01–3.00 V vs. Na⁺/Na. Electrochemical impedance spectroscopy (EIS) was also performed on a CHI 660a electrochemical workstation with a frequency range of 0.01 Hz to 100 kHz.

2.4. Co K-edge XAFS and O K-edge sXAS characterizations

Hard X-ray absorption fine structure (XAFS) spectra at Co K edge (E₀ = 7709 eV) were monitored at beamline BL14W1 of the Shanghai Synchrotron Radiation Facility (SSRF), operating at 3.5 GeV under “top-up” mode with a constant current of 220 mA [40]. The XAFS data were collected under transmission mode with ion chambers and the energy was calibrated according to the absorption edge of pure Co foil. Athena and Artemis code were used to extract the data and fit the profile [41,42]. For the X-ray absorption near edge structure (XANES) part, the experimental absorption coefficients as function of energies μ(E) were processed by background subtraction and normalization procedures, and showed as “normalized absorption”. For the extended X-ray absorption fine structure (EXAFS) part, the Fourier transformed (FT) data in R space were analyzed by applying metallic Co, CoO, Co₃O₄, and first-shell approximation models for Co-Co and Co-O shells. The passive electron factors, S₀², were determined by fitting the experimental Co foil data and fixing the Co-Co coordination number (CN) to be 12, and then fixed for further analysis of the measured samples. The parameters describing the electronic properties, e.g., correction to the photoelectron energy origin, E₀, and local structure environment including CN, distance (R), and Debye Waller (D. W.) factor around the absorbing atoms were allowed to vary during the fit process. The fitted ranges for k and R spaces were selected to be k = 3–12 Å⁻¹ and R = 1–3.8 Å (k³-weighted), respectively.

Soft X-ray absorption spectra (sXAS) were performed at beamline BL08UA of the SSRF. O K-edge sXAS spectra were recorded in the total electron yield (TEY) mode. The cycled u-CoOHtp samples under given states-of-charge (SOC) were collected by disassembling the coin cells inside an argon-filled glovebox, and subsequently rinsed with DGM for several times to remove the residual electrolyte. The wet u-CoOHtp electrodes were dried at room temperature overnight in argon-filled glovebox before XAFS and sXAS tests.

3. Results and discussion

b-CoOHtp and u-CoOHtp MOFs were ingeniously synthesized through microwave-assisted solvothermal method and ultrasonic strategy by using CoCl₂·6H₂O and H₂tp (tp = terephthalate) as the metal source and bridging ligand, respectively (see in the Section 2 for

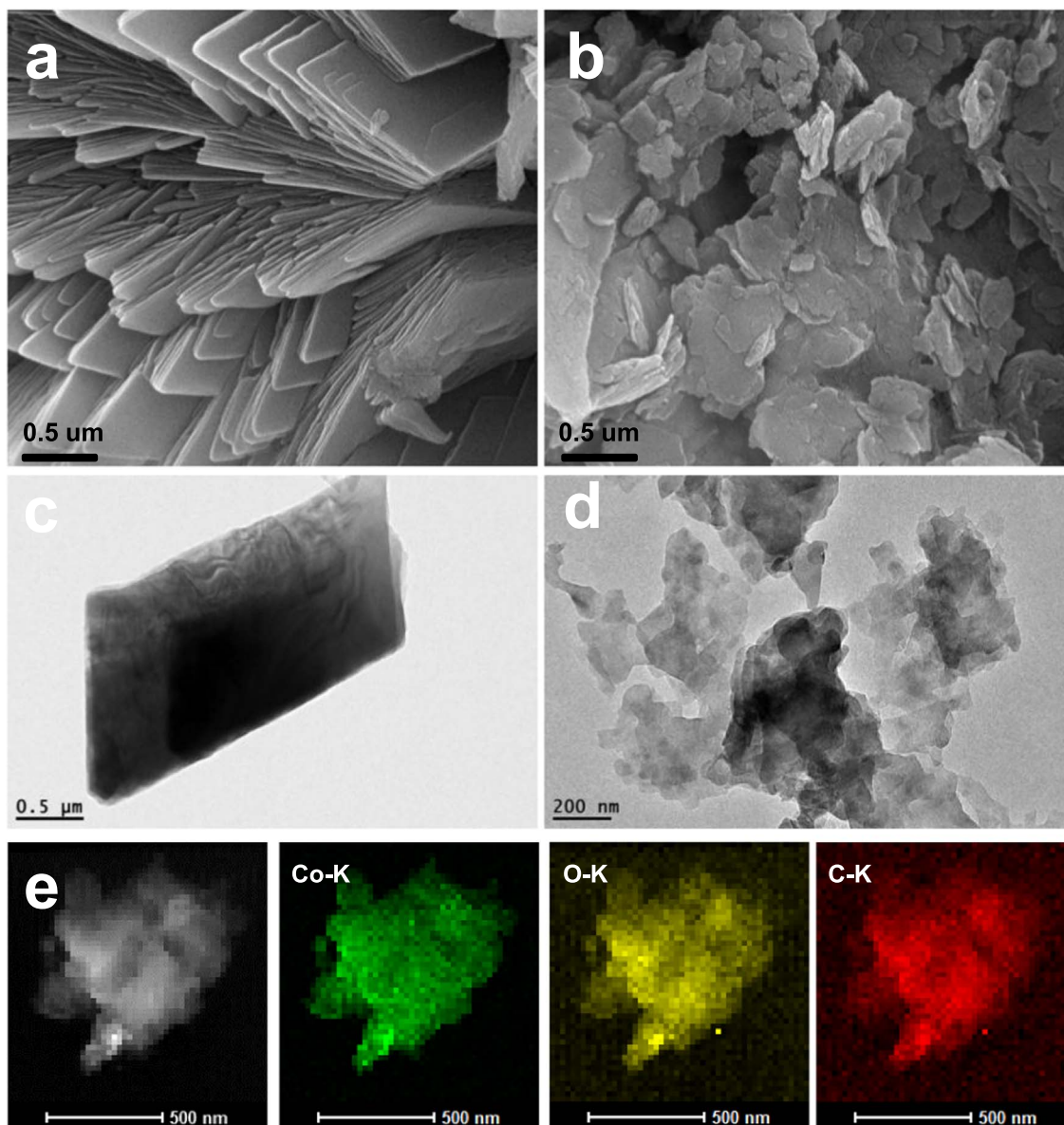


Fig. 1. (a, b) SEM micrographs of the obtained b-CoOHtp and u-CoOHtp MOFs, respectively. (c, d) TEM images of the as-prepared b-CoOHtp and u-CoOHtp MOFs, respectively. (e) STEM and the corresponding EDS mapping images of the as-synthesized u-CoOHtp, displaying the uniform distribution of Co, O, and C elements.

details). The morphology and microstructure of the obtained b-CoOHtp and u-CoOHtp MOFs were firstly examined by SEM, as displayed in Fig. 1a and b. The b-CoOHtp presents micron-grade crystals with lamellar crystalline architecture, whereas the u-CoOHtp is composed by densely accumulated and randomly assembled ultrathin nanosheets. The TEM image of b-CoOHtp in Fig. 1c further proves its lamellar architecture with solid and dense nature. In contrast, u-CoOHtp shows significantly different nanosheet structure, which are densely stacked and intimately interconnected (Fig. 1d). AFM analysis in Fig. 2a confirms that the thickness of u-CoOHtp is in the range of 1.4–3.5 nm, further demonstrating the ultrathin lamellar nanoarchitecture of u-CoOHtp.

The crystal structures of b-CoOHtp and u-CoOHtp MOFs were investigated via XRD, as presented in Fig. 2b. The XRD pattern of b-CoOHtp coincides well with that of the simulation based on the $\text{Co}_2(\text{OH})_2\text{tp}$ single crystal data (space group: $C2/m$, $a = 19.943(1) \text{ \AA}$, $b = 3.2898(1) \text{ \AA}$, $c = 6.2896(3) \text{ \AA}$, $\beta = 95.746^\circ(3)$, $V = 410.54 \text{ \AA}^3(3)$) [43], suggesting that a pure-phased crystal was obtained. The crystal texture of $\text{Co}_2(\text{OH})_2\text{tp}$ is layered and contains two types of octahedral-coordination Co^{2+} sites (each Co1 is coordinated with two μ_3 -OH and

four O-carboxylate atoms, whereas each Co2 is coordinated with four μ_3 -OH and two O-carboxylate atoms), as depicted in Fig. S1. The two kinds of edge-sharing CoO_6 polyhedrons are jointed with each other in the (200) facet to form metallic layers that are further connected together by terephthalate bridges [43]. The similar XRD pattern of u-CoOHtp with that of b-CoOHtp suggests that they are isostructural. However, the diffraction peaks are weaker and broader, demonstrating its poorer crystallinity and smaller crystallite size, which corresponds well with its ultrathin nanosheet microstructure. Besides, the diffraction peaks are shifted to the direction of low 2θ angle for u-CoOHtp (Fig. 2b, inset), indicating the presence of structural defects/disorder in u-CoOHtp. The atomic defects/disorder might affect the electronic structure of u-CoOHtp, thus tailoring the electrochemical property. Fig. S2a demonstrates the FT-IR spectra of the as-synthesized b-CoOHtp and u-CoOHtp MOFs, both of which exhibit the $\nu_{\text{as}}(\text{O}-\text{C}=\text{O})$ (1583 cm^{-1}) and $\nu_{\text{s}}(\text{O}-\text{C}=\text{O})$ (1353 cm^{-1}) stretching vibrations of the terephthalate linker, as well as $\nu(\text{OH})$ stretching vibration (3601 cm^{-1}) in the lattice of $\text{Co}_2(\text{OH})_2\text{tp}$. The thermal behavior was examined by TGA, as displayed in Fig. S2b. The decomposition of the bridging ligands begins at 424°C and finishes at 550°C for both b-CoOHtp and

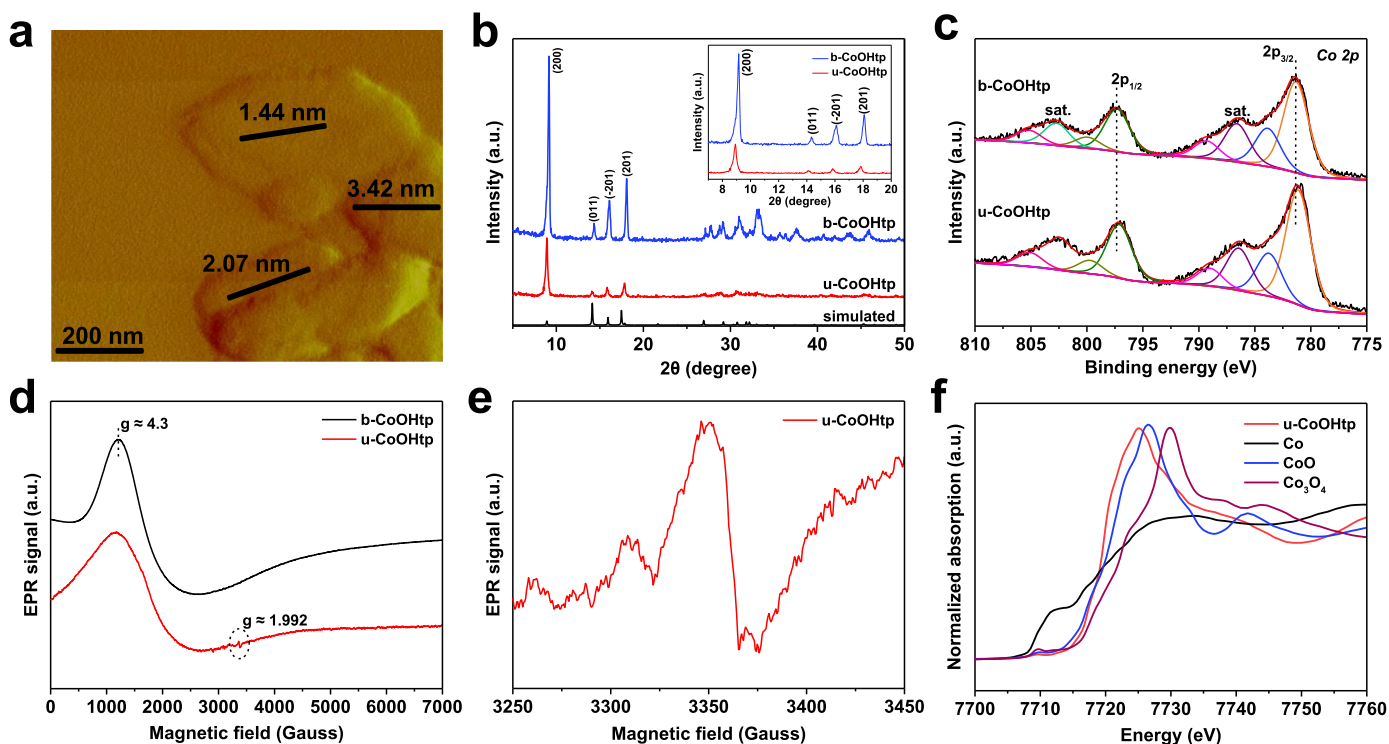


Fig. 2. (a) AFM image of the obtained u-CoOHtp, demonstrating the ultrathin characteristic of the nanosheets (1.4–3.5 nm). (b) XRD patterns of the as-synthesized b-CoOHtp, u-CoOHtp, and the simulated one. Inset: the enlarged XRD patterns in the 2θ range of 7–20°. (c) High-resolution Co 2p XPS spectra of b-CoOHtp and u-CoOHtp. (d) Continuous-wave X-band EPR spectra of b-CoOHtp and u-CoOHtp recorded under 2 K. (e) Fine scanning X-band EPR spectra of u-CoOHtp in the region of 3250–3450 G. (f) XANES spectrum of u-CoOHtp and the reference Co, CoO, and Co_3O_4 .

u-CoOHtp, demonstrating their high thermal stability. The BET surface areas of b-CoOHtp and u-CoOHtp measured from N_2 adsorption-desorption isotherms (Fig. S3a and b) are 5.8 and $11.5 \text{ m}^2 \text{ g}^{-1}$, respectively, suggesting a relatively low porosity.

Subsequent composition analyses by XPS survey spectra confirm that both b-CoOHtp and u-CoOHtp are composed of Co, O, and C elements without other impurities (Fig. S4a and b). Beyond that, the STEM-EDS mapping images of u-CoOHtp in Fig. 1e shows uniform distribution of Co, O, and C elements throughout the entire u-CoOHtp surface, further demonstrating the uniform composition. Fig. 2c presents the high-resolution Co 2p spectra of the as-prepared b-CoOHtp and u-CoOHtp, in which the typical $2p_{1/2}$ and Co $2p_{3/2}$ peaks for b-CoOHtp are located at 797.33 and 781.34 eV, respectively, accompanied by two evident satellite peaks beside them, demonstrating the existence of Co^{2+} in b-CoOHtp. Intriguingly, a blue shift of Co 2p XPS peaks to lower binding energy (about 0.17 eV) is observed for u-CoOHtp, which might be ascribed to the bond distortion between Co-O atoms in the ultrathin nanosheets, accompanying with the redistribution of electron density.

Further information about the electronic states was provided by continuous-wave EPR spectra at 2 K, as presented in Fig. 2d. The EPR spectra of b-CoOHtp and u-CoOHtp both contain a broad derivative lineshape with peak intensity around $g \sim 4.3$, which can be attributed to rhombic high-spin Co^{2+} ($t_{2g}^5 e_g^2$, $S = 3/2$) [44,45]. Moreover, a weak EPR signal with a g -value (1.992) that smaller than that of free electron ($g_e = 2.0023$) can be detected for u-CoOHtp, which is characteristic for oxygen vacancies [46]. The fine scanning around this region (3250–3450 G) in Fig. 2e further proves the EPR signal of oxygen vacancies, corresponding well with the Co 2p XPS result. The XANES region in XAFS responds to the electronic structure of the tested Co atoms was also shown in Fig. 2f. The edge energy, the white line intensity, and the pre-edge features are related to the oxidation state of $\text{Co}^{3+}/\text{Co}^{2+}/\text{Co}^0$. By comparing with the spectra of standard Co foil, CoO, and Co_3O_4 , the average valence state of Co-ions in the as-synthesized u-CoOHtp is

close to 2+.

On the basis of the above observations and analyses, it is reasonable to draw the following conclusions and conjectures: (1) Ultrathin $\text{Co}_2(\text{OH})_2\text{tp}$ nanosheets with thicknesses lower than 3.5 nm can be fabricated by a facile ultrasonic procedure. (2) The layered structure of u-CoOHtp with nanometer thicknesses is able to provide a short ion/electron migration path to the internal electroactive sites, thus resulting in rapid Na^+ diffusion [47,48]. (3) Self-adaptive oxygen vacancies are generated during the ultrathinning process of u-CoOHtp, which will incur an imbalanced charge distribution and produce local electric field [49,50]. Such in-plane built-in electric field might further accelerate charge transport kinetics by Coulomb forces and help to maintain the integrity of the electrode, thus achieving ameliorative Na-storage performance.

As a proof-of-concept, the electrochemical properties of b-CoOHtp and u-CoOHtp in SIBs were gauged, as summarized in Fig. 3. Fig. 3a shows the galvanostatic discharge-charge voltage profiles for the 1st and 10th cycle within the potential window of 3.00–0.01 V (*vs.* Na^+/Na) at current density of 50 mA g^{-1} . The first discharge profiles of b-CoOHtp and u-CoOHtp both comprise a dominant plateau as well as a sloping region, corresponding to an initial discharge capacity of 671 and 774 mA h g^{-1} , respectively. However, the discharge plateau is higher in the case of u-CoOHtp, demonstrating the influence of microstructure to the electrochemical behavior, which has also been reflected from the CV peaks in Fig. S5a. The relatively small initial Coulombic efficiency (ICE) of b-CoOHtp and u-CoOHtp (54.7% and 75.3%, respectively) might be ascribed to the irreversible decomposition of electrolyte, the inevitable formation of solid-state interphase (SEI) membrane, and partial Na^+ trapping in the electroactive sites [51]. After electrochemical activation for 10 cycles, the shapes of discharge profiles (Fig. 3a) and CV curves (Fig. S5b) become analogous for b-CoOHtp and u-CoOHtp, indicating that similar electrochemical reactions are occurred in these two electrodes. Besides, the discharge capacities for u-CoOHtp and b-CoOHtp in the 10th cycle are 418 and

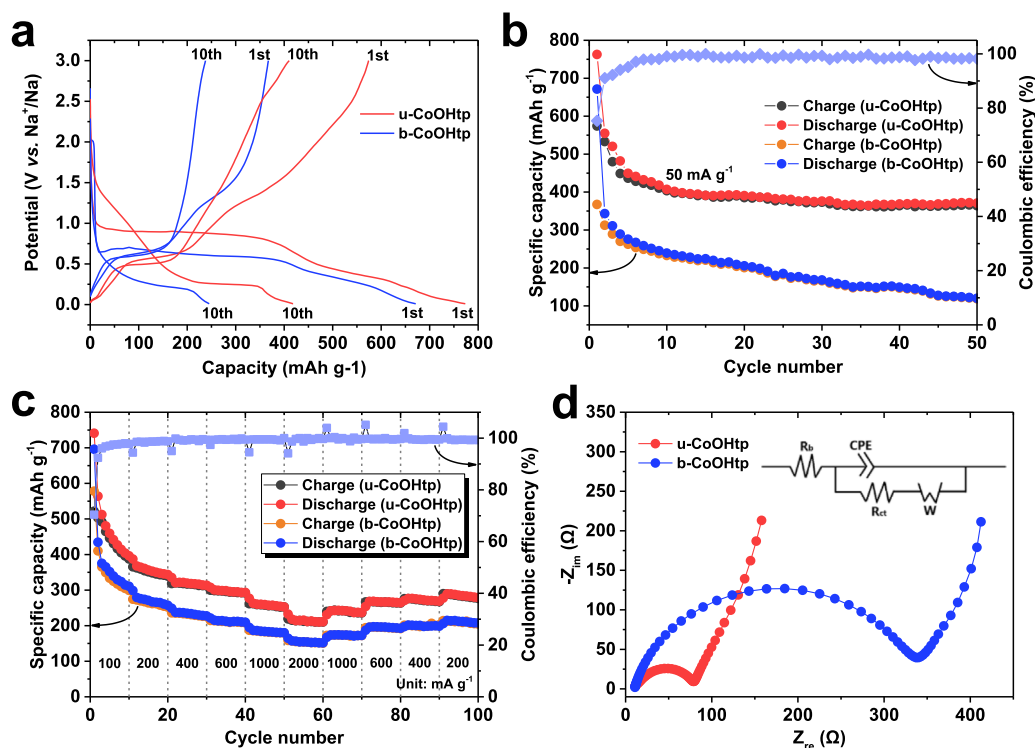


Fig. 3. Electrochemical performance of b-CoOHtp and u-CoOHtp in Na half-cells: (a) galvanostatic discharge-charge voltage profiles for the 1st and 10th cycle within the potential window of 3.00–0.01 V vs. Na⁺/Na; (b) cycling performances at a current density of 50 mA g⁻¹; (c) rate performances at various current rates from 100 to 2000 mA g⁻¹; (d) electrochemical impedance spectra after the initial cycle.

245 mA h g⁻¹, respectively, suggesting the improved reversibility of Na intercalation/extraction processes for u-CoOHtp with an ultrathin nanosheet microstructure.

Fig. 3b displays the cycling performances of u-CoOHtp and b-CoOHtp at a current density of 50 mA g⁻¹. The u-CoOHtp electrode exhibits superior cyclability and a reversible capacity of 371 mA h g⁻¹ is retained after 50 cycles, with Coulombic efficiency approaching 100%. In contrast, the specific capacity of b-CoOHtp rapidly declines and remains at only 119 mA h g⁻¹ after 50 cycles. The rate capability was then evaluated, as presented in Fig. 3c. It can be clearly observed that u-CoOHtp exhibits higher capacity retention under the same current rate in comparison to b-CoOHtp (~442, ~358, ~320, ~298, ~260, and ~215 mA h g⁻¹ at current densities of 100, 200, 400, 600, 1000, and 2000 mA g⁻¹, respectively), further demonstrating the ameliorative Na-storage performance of u-CoOHtp. However, when the current rate is gradually resumed from 2000 to 200 mA g⁻¹, the charge/discharge cycles at the same rates seem to be less stable for both u-CoOHtp and b-CoOHtp. We attribute this phenomenon to the intrinsic low electrical conductivity of MOFs that cannot be overcome by ultrathinning treatment. Considering on the relatively high capacity of u-CoOHtp under the 1st and 2nd cycle (763 and 555 mA h g⁻¹, respectively), it can be anticipated that the Na-storage performance of u-CoOHtp could be further improved by covalent stitching with conductive scaffold such as two-dimensional graphene.

The performance superiority of u-CoOHtp over b-CoOHtp could probably ascribed to the unique ultrathin nanosheet architecture. Firstly, the layered structure of u-CoOHtp with nanometer thicknesses can provide shortened ion/electron transport paths to the internal electroactive sites, giving rise to rapid Na⁺ diffusion [47,48]. Secondly, the ultrathinning process of u-CoOHtp might create unsaturated coordination metal sites on the exposed surfaces because the bridges between surface metal cations and terephthalate ligands are partially terminated, thus resulting in improved metal redox activity [39]. Finally, self-adaptive oxygen vacancies are generated in u-CoOHtp with atomic-scale thicknesses, which would then cause imbalanced

charge distribution and create local electric field. Such built-in electric field would further accelerate Na⁺ migration rates and help to maintain the integrity of the electrode, thus achieving enhanced reversibility of the Na intercalation/extraction processes [49,50].

To monitor the local structure and valence state evolution of the u-CoOHtp electrode during charge/discharge processes, the ex-situ XAFS spectra were performed at various states-of-charge (SOC). Fig. 4a and b present the ex-situ Co K-edge XANES spectra during the first discharge and charge process, respectively. When the discharge process is proceeding, the Co K-edge XANES spectra continuously shift toward the K-edge position of Co foil, implying the reduction of the oxidation state of Co in the u-CoOHtp sample. More specifically, the intensity of pre-edge peaks significantly increases before 0.4 V, but becomes nearly unchanged between 0.4–0.01 V, indicating that the decrease of the oxidation state of Co mainly occurs between 3.0–0.4 V. The overall Co K-edge lineshape of the full-discharged u-CoOHtp sample is close to that of Co foil, which indicates the occurrence of Co⁰ during the Na-intercalation process. During the charge process, the Co K-edge can shift back toward the position of CoO, demonstrating the progressive recovery of Co²⁺. However, the overall K-edge lineshape of the full-charged u-CoOHtp sample is different from that of pristine u-CoOHtp, suggesting that the local coordination environment around Co atoms cannot completely recover during charge process. In addition, the Co K-edge XANES spectrum of the u-CoOHtp sample after 20 cycles is also performed and displayed in Fig. 4b, which is almost identical to that of the full-charged u-CoOHtp sample after 1 cycle, demonstrating the reversibility of Na⁺ intercalation/extraction process after the activation cycle.

To shed more light on the local structure evolution of u-CoOHtp, the EXAFS part with the profile fitting in R space was carried out to determine the short-range local structure including distances (R) and coordination number (CN) around the studied Co atoms. The EXAFS pattern (Fig. 4c and d and Table 1) exhibits a strong peak at ~2.08 Å (phase shift corrected) with a CN of 7.0 (±0.6) for the pristine u-CoOHtp, which is associated with Co–O interaction in the first

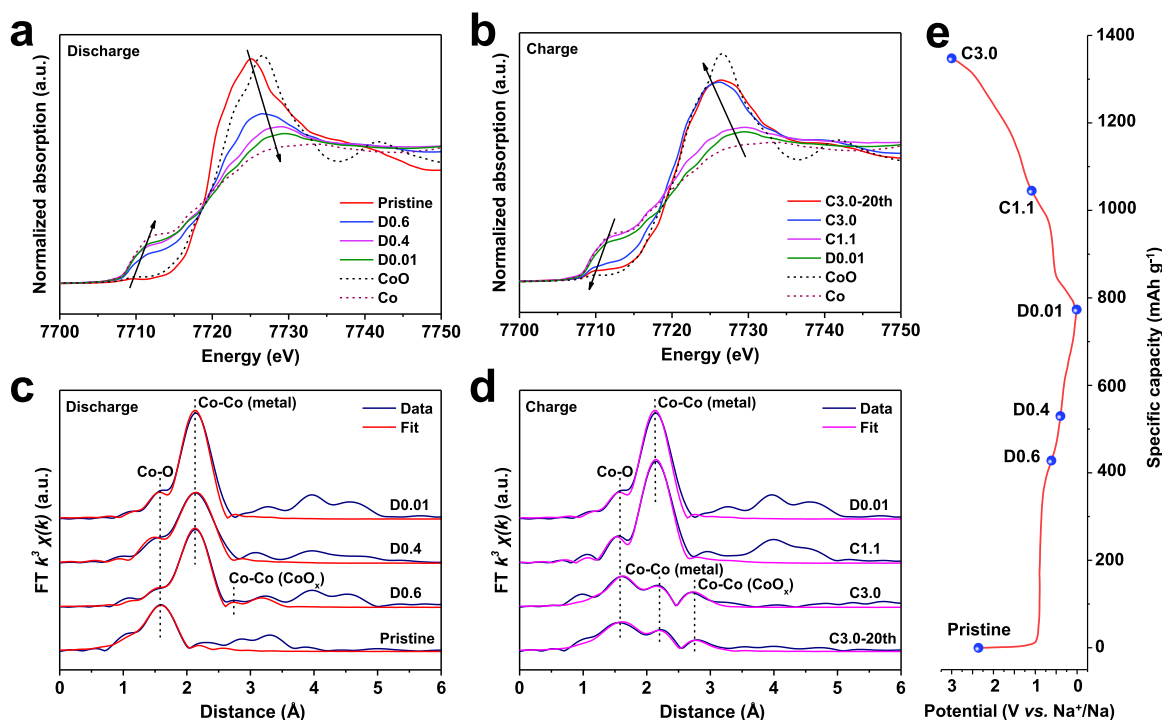


Fig. 4. (a, b) Co K-edge XANES spectra of u-CoOHtp at various states-of-charge during the first discharge and charge (including the 20th cycle) process, respectively. (c, d) EXAFS patterns of u-CoOHtp at various states-of-charge during the first discharge and charge (including the 20th cycle) process, respectively. (e) The corresponding electrochemistry profile in the potential window of 3.0–0.01 V (vs. Na⁺/Na) under a current density of 50 mA g⁻¹.

Table 1

Co K-edge EXAFS fitting results (R: distance, CN: coordination number) of u-CoOHtp at various states-of-charge (phase shift corrected).

Sample	Co-O		Co-Co	
	R (Å)	CN	R (Å)	CN
Co	–	–	2.491	12
CoO	2.132	6	3.014	12
Co ₃ O ₄	1.943	6	2.874	6
			3.370	6
Pristine	2.08 ± 0.01	7.0 ± 0.6	–	–
D0.6	2.00 ± 0.02	1.7 ± 0.6	2.49 ± 0.01	4.8 ± 0.6
			3.14 ± 0.04	0.8 ± 0.4
D0.4	1.93 ± 0.03	1.1 ± 0.7	2.48 ± 0.02	5.4 ± 1.1
D0.01	1.89 ± 0.03	0.9 ± 0.3	2.49 ± 0.01	6.2 ± 0.3
C1.1	1.90 ± 0.03	0.6 ± 0.3	2.48 ± 0.01	5.2 ± 0.8
C3.0	2.04 ± 0.01	3.2 ± 0.2	2.48 ± 0.01	1.9 ± 0.3
			3.12 ± 0.01	2.2 ± 0.4
C3.0–20th	2.04 ± 0.02	4.1 ± 0.7	2.50 ± 0.01	1.6 ± 0.6
			3.11 ± 0.03	1.2 ± 0.6

coordination shell [52]. Additionally, the CN agrees well with the crystal structure of u-CoOHtp [43]. After discharging to 0.6 V, the intensity of first shell of Co–O decreases drastically, while a new main peak located at ~ 2.49 Å along with a weak peak at ~ 3.14 Å appears, which can be assigned to the two second shells of Co–Co interaction (metallic Co and CoO_x, respectively) [53,54]. Furthermore, the intensity of Co–Co peak at ~ 2.49 Å (metallic Co) becomes stronger after deeper sodiation to 0.01 V, while the Co–O peak does not disappear, indicating that this stage is a mixed phase containing MOF skeleton and nanosized metallic Co. When the charge process is proceeding, the strong and only Co–Co peak at ~ 2.49 Å gradually decreases and split into two second shells of Co–Co (R: 2.47–2.51 and 3.08–3.14 Å), suggesting the occurrence of CoO_x species (0 < x < 1). The intensities of the two Co–Co peaks are much weaker than that of the full-discharged u-CoOHtp, and the intensity of the Co–O peak is also weaker than that of pristine u-CoOHtp. Hence, the full-charge u-CoOHtp sample should

be a mixed phase of Co-MOF, CoO_x species, and nanosized metallic Co. The presence of CoO_x species in the full-charge u-CoOHtp can also be observed via HRTEM, as depicted in Fig. S6a and b. The EXAFS patterns of the u-CoOHtp sample after 1 and 20 cycles are almost identical, which is in good agreement with the XANES result (Fig. 4b), further proving that the Na⁺ intercalation/extraction processes after the activation cycle is reversible. It can also clearly be seen in Table 1 that the Co–O distance and the corresponding CN decrease gradually during the discharge process, and then continuously increase during the charge process. In comparison, the CN of Co–Co (metallic Co) gradually increase upon discharge and then decrease upon charge.

Ex-situ sXAS spectra at the O K-edge were also performed to monitor the local structure evolution of the u-CoOHtp series in greater detail, as shown in Fig. 5. The pre-edge region in the energy range of 528–534 eV is associated with the spectroscopic excitations of O 1s electrons to O-2p/Co-3d hybridized orbitals, while the main-peak region between 535 and 546 eV corresponds to the excitations to O-2p/Co-4sp hybridized orbitals [45]. The pre-edge peaks are very sensitive to the local environment variation around oxygen ions [54–56]. In contrast with the evolution process of Co K-edge (XANES and EXAFS), the O K-edge sXAS spectra of the cycled u-CoOHtp does not show evident changes when the discharge process is proceeding to 0.4 V. However, further Na⁺ intercalation to 0.01 V gives rise to the formation of a new absorption peak at the energy lower than the pre-edge peak of pristine u-CoOHtp (p2: 530.63 eV, p1: 531.79). The pre-edge shift to lower photon energy indicates that more Na-ions are captured by the carboxyl O-ions with high electronegativity between 0.4–0.01 V, and the bond covalence of O-2p/Co-3d hybridized orbitals would decrease as the same time [55,57]. When the charge process is proceeding, the intensity of p2 peak decays, while the intensity of p1 peak increases gradually, and then the O K-edge sXAS spectra are almost identical to that of pristine u-CoOHtp during the subsequent charge process. Hence, it is reasonable to conclude that extra Na-ions can be reversibly intercalated and extracted to/from the carboxyl oxygen atoms of u-CoOHtp in the low voltage region.

Based on the above spectroscopic observations and analyses, the

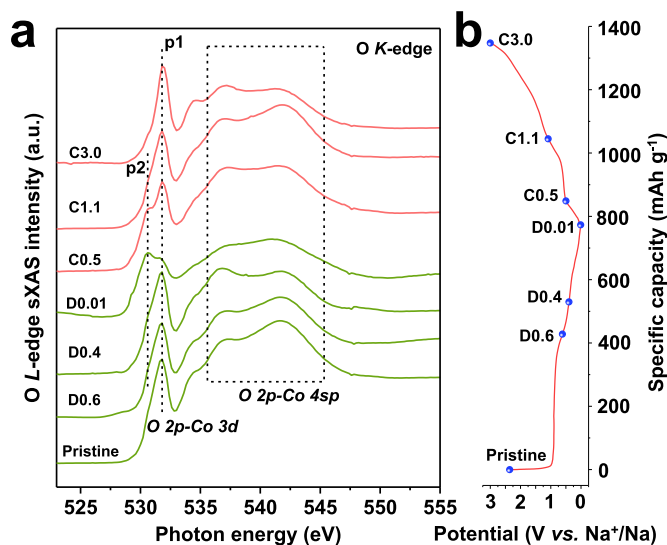


Fig. 5. (a) O K-edge sXAS spectra of u-CoOHtp at various states-of-charge during the first discharge and charge processes. (b) The corresponding electrochemistry profile in the potential window of 3.0–0.01 V (*vs.* Na⁺/Na) under a current density of 50 mA g⁻¹.

detailed Na⁺ intercalation/extraction mechanism of u-CoOHtp was proposed. When the discharge process is proceeding, the u-CoOHtp firstly undergoes a reduction between Co²⁺ and Co⁰, corresponding to the discharge region above 0.4 V (*vs.* Na⁺/Na). Then, additional Na ions are inserted to the coordinated carboxyl oxygen atoms with high electronegativity, representing the discharge region below 0.4 V. During the charge process, the electrode firstly undergoes the Na⁺ extraction process from the carboxyl oxygen atoms (below 1.1 V), followed by the oxidation process of Co⁰ to Co²⁺. It should be underlined that the structure of pristine u-CoOHtp is not recovered during charge process, and this stage is a mixed phase containing Co-MOF, CoO_x species, and nanosized Co⁰, as proved by the XANES and EXAFS results. This mixed-phase sample is reversible during the subsequent electrochemical process, which ensures a stable capacity of about 400 mA h g⁻¹ during repeated cycles. The Na⁺ intercalation/extraction mechanism suggested here agrees well with the CV results (Fig. S5a and b). More detailed investigation of the Na⁺ intercalation/extraction mechanism in the subsequent cycles is still in progress. To the best of our knowledge, such comprehensive understanding on the electrochemical Na⁺ intercalation/extraction mechanism of MOF-based materials at atomic level has never been reported before. Further enhancement on the Na-storage performance of u-CoOHtp might be possible by grafting with conductive scaffold such as two-dimensional graphene.

4. Conclusion

In summary, we have introduced self-adaptive oxygen vacancies in Co₂(OH)₂tp MOF nanosheets (u-CoOHtp) via a facile and ingenious ultrasonic approach. In this system, the ultrathin nanosheet configuration can not only provide abundant electroactive sites to ensure a high Na-storage capacity, but also offer short ion/electron diffusion path to the internal active sites. More importantly, the self-adaptive oxygen vacancies generated would create in-plane local electric field, which could accelerate Na⁺/e⁻ migration rates and promote the charge transfer behavior. Benefitting from the multiple structural advantages, the u-CoOHtp is able to deliver a reversible capacity of 555 mA h g⁻¹ at 50 mA g⁻¹ and maintain remarkable cyclic performance (371 mA h g⁻¹ after 50 cycles). Furthermore, the electronic state and local environment evolution of the u-CoOHtp electrode during cycling were studied by a combination of XAFS and sXAS techniques. The results prove that:

(i) the pristine u-CoOHtp is converted to a mixed phase containing Co-MOF, CoO_x species and nanosized Co⁰ after the first cycle; (ii) Co²⁺ and metallic Co are interchangeable during repeated cycling; (iii) a certain portion of charge compensation during Na⁺ intercalation/extraction is achieved on the carboxyl oxygen sites. We believe our in-depth understanding on the Na⁺ intercalation/extraction mechanism of MOFs achieved here will shed new light on their advancement in sodium-ion batteries.

Acknowledgements

This work was supported by National Natural Science Foundation of China and that for Excellent Young Scholars (Nos. 21522303, 21703068). We also acknowledge the support from Shanghai Synchrotron Radiation Facility (BL14W1, BL08UA) for the XAFS and sXAS experiments. C. L. is grateful to ECNU Outstanding Doctoral Dissertation Cultivation Plan of Action (No. YB2016031).

Appendix A. Supplementary material

Supplementary data associated with this article can be found in the online version at doi:10.1016/j.jensm.2018.02.021.

References

- [1] V. Palomares, M. Casas-Cabanas, E. Castillo-Martinez, M.H. Han, T. Rojo, *Energy Environ. Sci.* 6 (2013) 2312–2337.
- [2] M.D. Slater, D. Kim, E. Lee, C.S. Johnson, *Adv. Funct. Mater.* 23 (2013) 947–958.
- [3] S.Y. Hong, Y. Kim, Y. Park, A. Choi, N. Choi, K.T. Lee, *Energy Environ. Sci.* 6 (2013) 267–281.
- [4] S. Kim, D. Seo, X. Ma, G. Ceder, K. Kang, *Adv. Energy Mater.* 2 (2012) 710–721.
- [5] H. Pan, Y. Hu, L. Chen, *Energy Environ. Sci.* 6 (2013) 2338.
- [6] E. Irisarri, A. Ponrouch, M.R. Palacin, *J. Electrochem. Soc.* 162 (2015) A2476–A2482.
- [7] Y. Li, Y. Lu, C. Zhao, Y. Hu, M. Titirici, H. Li, X. Huang, L. Chen, *Energy Storage Mater.* 7 (2017) 130–151.
- [8] Y. Li, Y. Hu, X. Qi, X. Rong, H. Li, X. Huang, L. Chen, *Energy Storage Mater.* 5 (2016) 191–197.
- [9] J.L.C. Rowsell, O.M. Yaghi, *Microporous Mesoporous Mater.* 73 (2004) 3–14.
- [10] H. Furukawa, K.E. Cordova, M. O’Keeffe, O.M. Yaghi, *Science* 341 (2013) 1230–1234.
- [11] B. Li, H. Wen, Y. Cui, W. Zhou, G. Qian, B. Chen, *Adv. Mater.* 28 (2016) 8819–8860.
- [12] Y. Zhao, Z. Song, X. Li, Q. Sun, N. Cheng, S. Lawes, X. Sun, *Energy Storage Mater.* 2 (2016) 35–62.
- [13] Z. Liang, C. Qu, W. Guo, R. Zou, Q. Xu, *Adv. Mater.* (2017) 1702891.
- [14] X. Li, F. Cheng, S. Zhang, J. Chen, *J. Power Sources* 160 (2006) 542–547.
- [15] C. Li, X. Hu, X. Lou, L. Zhang, Y. Wang, J. Amoureux, M. Shen, Q. Chen, B. Hu, *J. Mater. Chem. A* 4 (2016) 16245–16251.
- [16] C. Li, X. Hu, W. Tong, W. Yan, X. Lou, M. Shen, B. Hu, *ACS Appl. Mater. Interfaces* 9 (2017) 29829–29838.
- [17] C. Li, X. Lou, M. Shen, X. Hu, Z. Guo, Y. Wang, B. Hu, Q. Chen, *ACS Appl. Mater. Interfaces* 8 (2016) 15352–15360.
- [18] Z. Zhang, H. Yoshikawa, K. Awaga, *Chem. Mater.* 28 (2016) 1298–1303.
- [19] Z. Zhang, H. Yoshikawa, K. Awaga, *J. Am. Chem. Soc.* 136 (2014) 16112–16115.
- [20] G. Férey, F. Millange, M. Morcrette, C. Serre, M. Doublet, J. Grenèche, J. Tarascon, *Angew. Chem. Int. Ed.* 119 (2007) 3323–3327.
- [21] D. Wu, Z. Guo, X. Yin, Q. Pang, B. Tu, L. Zhang, Y. Wang, Q. Li, *Adv. Mater.* 26 (2014) 3258–3262.
- [22] J. Zheng, J. Tian, D. Wu, M. Gu, W. Xu, C. Wang, F. Gao, M.H. Engelhard, J. Zhang, J. Liu, J. Xiao, *Nano Lett.* 14 (2014) 2345–2352.
- [23] J. Zhou, R. Li, X. Fan, Y. Chen, R. Han, W. Li, J. Zheng, B. Wang, X. Li, *Energy Environ. Sci.* 7 (2014) 2715.
- [24] Z. Peng, X. Yi, Z. Liu, J. Shang, D. Wang, *ACS Appl. Mater. Interfaces* 8 (2016) 14578–14585.
- [25] L. Wang, Y. Han, X. Feng, J. Zhou, P. Qi, B. Wang, *Coord. Chem. Rev.* 307 (2016) 361–381.
- [26] K.M. Choi, H.M. Jeong, J.H. Park, Y. Zhang, J.K. Kang, O.M. Yaghi, *ACS Nano* 8 (2014) 7451–7457.
- [27] X. Liu, C. Shi, C. Zhai, M. Cheng, Q. Liu, G. Wang, *ACS Appl. Mater. Interfaces* 8 (2016) 4585–4591.
- [28] D. Sheberla, J.C. Bachman, J.S. Elias, C. Sun, Y. Shao-Horn, M. Dincă, *Nat. Mater.* 16 (2016) 220–224.
- [29] Y. Ning, X. Lou, M. Shen, B. Hu, *Mater. Lett.* 197 (2017) 245–248.
- [30] C. Dong, L. Xu, *ACS Appl. Mater. Interfaces* 9 (2017) 7160–7168.
- [31] C. Fang, Y. Huang, L. Yuan, Y. Liu, W. Chen, Y. Huang, K. Chen, J. Han, Q. Liu, Y. Huang, *Angew. Chem. Int. Ed.* 56 (2017) 6793–6797.
- [32] S. He, X. Zhou, Z. Li, J. Wang, L. Ma, S. Yang, *ACS Appl. Mater. Interfaces* 9 (2017) 26907–26914.

- [33] L. Shen, H. Song, C. Wang, *Electrochim. Acta* 235 (2017) 595–603.
- [34] S. Maiti, A. Pramanik, U. Manju, S. Mahanty, *ACS Appl. Mater. Interfaces* 7 (2015) 16357–16363.
- [35] Q. Liu, L. Yu, Y. Wang, Y. Ji, J. Horvat, M. Cheng, X. Jia, G. Wang, *Inorg. Chem.* 52 (2013) 2817–2822.
- [36] H. Song, L. Shen, J. Wang, C. Wang, *Nano Energy* 34 (2017) 47–57.
- [37] O. Pecher, J. Carretero-González, K.J. Griffith, C.P. Grey, *Chem. Mater.* 29 (2016) 213–242.
- [38] X. Rong, J. Liu, E. Hu, Y. Liu, Y. Wang, J. Wu, X. Yu, K. Page, Y. Hu, W. Yang, H. Li, X. Yang, L. Chen, X. Huang, *Joule* 2 (2018) 125–140.
- [39] S. Zhao, Y. Wang, J. Dong, C. He, H. Yin, P. An, K. Zhao, X. Zhang, C. Gao, L. Zhang, J. Lv, J. Wang, J. Zhang, A.M. Khattak, N.A. Khan, Z. Wei, J. Zhang, S. Liu, H. Zhao, Z. Tang, *Nat. Energy* 1 (2016) 16184.
- [40] Y.U. Hai-Sheng, W. Xiang-Jun, L.I. Jiong, G.U. Song-Qi, Z. Shuo, *Nucl. Sci. Technol.* 26 (2015) 50102.
- [41] Q. Yang, X. Fu, C. Jia, C. Ma, X. Wang, J. Zeng, R. Si, Y. Zhang, C. Yan, *ACS Catal.* 6 (2016) 3072–3082.
- [42] W. Wang, P. Du, S. Zou, H. He, R. Wang, Z. Jin, S. Shi, Y. Huang, R. Si, Q. Song, C. Jia, C. Yan, *ACS Catal.* 5 (2015) 2088–2099.
- [43] Z. Huang, M. Drillon, N. Masciocchi, A. Sironi, J. Zhao, P. Rabu, P. Panissod, *Chem. Mater.* 12 (2000) 2805–2812.
- [44] B.M. Weckhuysen, A.A. Verberckmoes, M.G. Uytterhoeven, F.E. Mabbs, D. Collison, E. de Boer, R.A. Schoonheydt, *J. Phys. Chem. B* 104 (2000) 37–42.
- [45] C. Li, X. Lou, M. Shen, X. Hu, W. Yan, Y. Zou, W. Tong, B. Hu, *Energy Storage Mater.* 7 (2017) 195–202.
- [46] F. Lei, Y. Sun, K. Liu, S. Gao, L. Liang, B. Pan, Y. Xie, *J. Am. Chem. Soc.* 136 (2014) 6826–6829.
- [47] C. Yan, C. Lv, Y. Zhu, G. Chen, J. Sun, G. Yu, *Adv. Mater.* 29 (2017) 1703909.
- [48] Y. He, A. Muhetaer, J. Li, F. Wang, C. Liu, Q. Li, D. Xu, *Adv. Energy Mater.* 7 (2017) 1700950.
- [49] Y. Zheng, T. Zhou, X. Zhao, W.K. Pang, H. Gao, S. Li, Z. Zhou, H. Liu, Z. Guo, *Adv. Mater.* 29 (2017) 1700396.
- [50] Y. Liu, T. Zhou, Y. Zheng, Z. He, C. Xiao, W.K. Pang, W. Tong, Y. Zou, B. Pan, Z. Guo, Y. Xie, *ACS Nano* 11 (2017) 8519–8526.
- [51] M. Mao, F. Yan, C. Cui, J. Ma, M. Zhang, T. Wang, C. Wang, *Nano Lett.* 17 (2017) 3830–3836.
- [52] T. Deng, W. Zhang, O. Arcelus, J. Kim, J. Carrasco, S.J. Yoo, W. Zheng, J. Wang, H. Tian, H. Zhang, X. Cui, T. Rojo, *Nat. Commun.* 8 (2017) 15194.
- [53] X. Wang, L. Du, M. Du, C. Ma, J. Zeng, C. Jia, R. Si, *Phys. Chem. Chem. Phys.* 19 (2017) 14533–14542.
- [54] W. Yoon, M. Balasubramanian, K.Y. Chung, X. Yang, J. McBreen, C.P. Grey, D.A. Fischer, *J. Am. Chem. Soc.* 127 (2005) 17479–17487.
- [55] W. Yoon, K. Kim, M. Kim, M. Lee, H. Shin, J. Lee, J. Lee, C. Yo, *J. Phys. Chem. B* 106 (2002) 2526–2532.
- [56] W. Yoon, M. Balasubramanian, X. Yang, Z. Fu, D.A. Fischer, J. McBreen, *J. Electrochem. Soc.* 151 (2004) A246.
- [57] T. Glaser, K. Rose, S.E. Shadle, B. Hedman, K.O. Hodgson, E.I. Solomon, *J. Am. Chem. Soc.* 123 (2001) 442–454.